# Compact Modular Multi-Part Torsion Springs: Broadening the Design Space with Series Configurations

Zachary Bons[†,1,2,3], Yuanshao Yang[†,1,2,3] and Elliott J. Rouse[1,2,3]

***Abstract*—Springs are a vital component in many mechanical systems, where compactness and low mass are key. In a prior study, we demonstrated best-in-class energy density with a novel torsion spring, but it was fundamentally limited by its maximum allowable deflection. In this work, we present a novel series-connected torsion spring architecture that overcomes this constraint, enabling the realization of arbitrarily large deflection ranges in a highly compact and lightweight form factor. We introduce two modular series-connection designs and provide a nonlinear analytical model to account for backlash effects inherent in series connections. Experimental validation demonstrates the scalability and tunability of the proposed architecture, with measured stiffness closely matching designed values and a consistently low energy loss (∼5%). This approach broadens the design space for torsion springs, enabling new opportunities for lightweight, compact actuation across a wide range of robotic, automotive, and consumer applications.**

***Index Terms*—Torsion springs, compliant mechanisms, series elastic actuators, energy storage, backlash compensation.**

## I. INTRODUCTION

Springs, in their various forms, are ubiquitous in both natural and engineered mechanisms. They are a unique class of mechanical elements, governing the positional relationship between two (or more) objects while enabling energy storage and return, shock tolerance, compliant interactions, and the generation of restoring torques [1]. These features, among others, have resulted in widespread adoption across simple and complex devices, from watches to aircraft control surfaces to vehicle suspensions and door hinges [2]. Unfortunately, springs also add mass, volume, and complexity [3] to machine designs, which are often undesired attributes of most modern robotic systems. Consequentially, designers must balance the benefits and drawbacks of added elasticity, which often depends on application.

While existing applications of springs span a vast array of industries, the developing field of robotics—which often requires a system to carry its own actuator and battery mass—has made significant progress towards minimizing the drawbacks of springs in order to leverage their associated benefits. Gaining research traction following the development of series elastic actuation [1], novel torsion springs have been increasingly designed to be conveniently packaged alongside motors [4]–[6]. Of these, the most compact and lightweight torsion springs consisted of spiral-based designs [7]–[9], which offer a wide range of stiffness and deflection possibilities; however, when designed for large angular deflections, the spiral designs can only reliably be loaded in one direction [2], [7]. There is a gap in available spring design architectures that can achieve deflections beyond the small angles typically associated with torsion spring design (e.g. $<\sim$15 deg.); this limitation also inhibits the energy storage potential, which scales with the square of deflection.

In a previous study, we developed a novel, two-part torsion spring architecture that is best-in-class when considering energy storage per unit mass (specific energy) and per unit volume (energy density); however, it is limited in total allowable deflection [10]. The spring design leverages the efficient loading condition of cantilever beams arranged within a rotary architecture in order to store large amounts of energy within a compact and lightweight form factor (Fig. 1). In addition, we developed an openly-available design tool to reduce complexity and thus facilitate the design process [11]. The design can reliably render a wide range of stiffness coefficients with up to 20 degrees of deflection, but due to space constraints and small-angle approximations, it was not suitable for applications requiring larger deflection ranges. Thus, the design space is considerably restricted by the limit on total allowable deflection that stems from the contact limitations between two parts of the spring.

In this work, we resolve the deflection limitation by developing series configurations of the prior two-part spring design, which can be scaled to achieve arbitrarily large ranges of deflection. More specifically, the major contributions of this work include:

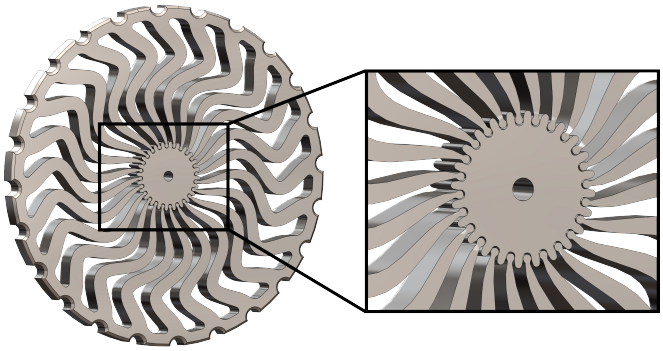

Fig. 1: The two-part spring design [10] is the most compact and lightweight torsion spring to date, but is limited to a maximum of ∼20 degrees of deflection.

[†]Co-first authors

[1] Neurobionics Lab, University of Michigan, Ann Arbor, USA

[2] Department of Mechanical Engineering, University of Michigan, Ann Arbor, USA {zbons, yuanshao, ejrouse}@umich.edu

[3] Department of Robotics, University of Michigan, Ann Arbor, USA

This work was supported by the National Science Foundation with the National Robotics Initiative under Grant 2024237 and Grant 1830338, and Division of Graduate Education under Grant 2241144.

Digital Object Identifier XX.XXXX/SRO.2022.XXXXXXX

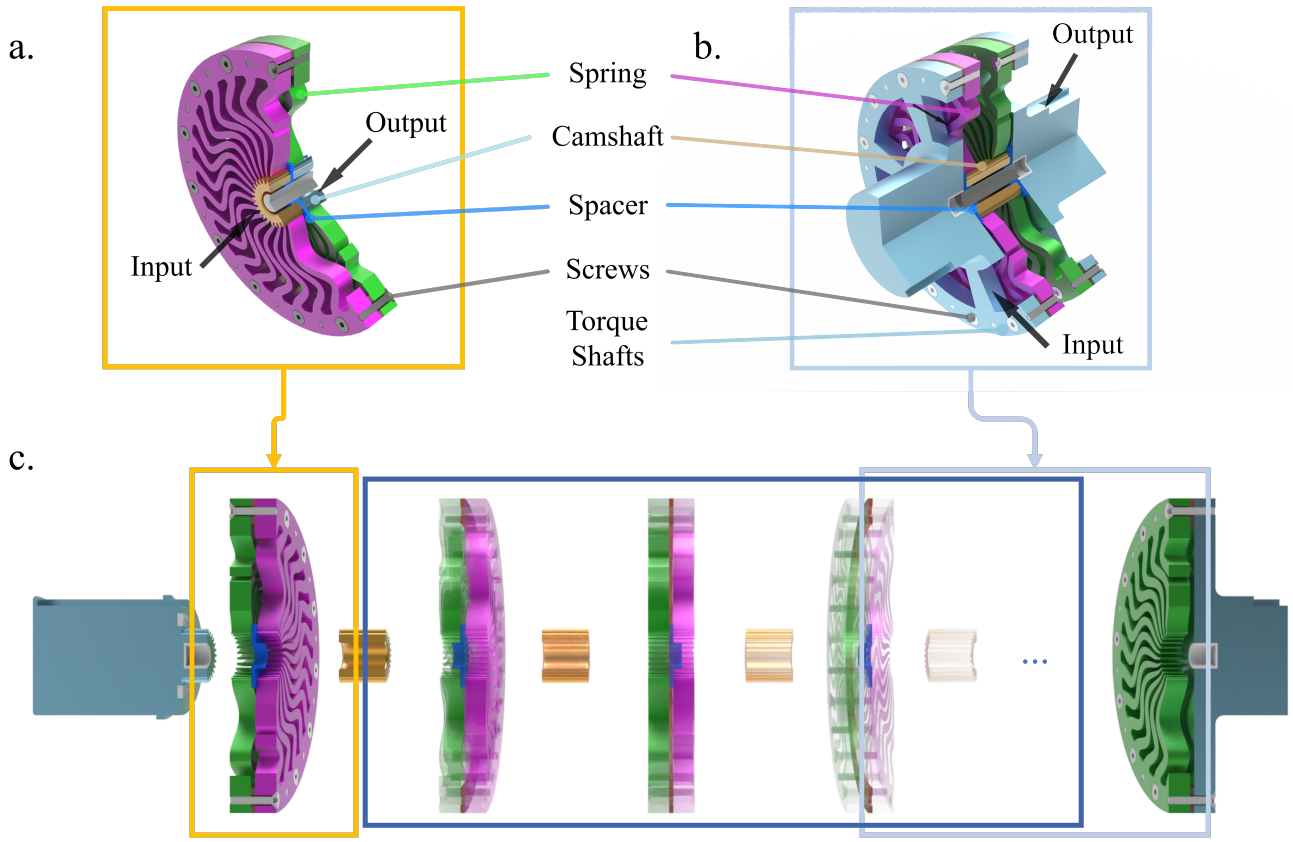


Fig. 2: Springs can be coupled in various series configurations to achieve large deflections in a compact and lightweight form-factor. **(a)** Two springs joined at the outer rim can be loaded via an input and output camshaft. Screws can rigidly connect the outer rims of the two springs, and the spacer prevents either camshaft from loading both springs in parallel. **(b)** Two springs sharing a common camshaft can be loaded via their outer rims. The attachment to the outer rim could be integrated with system components or achieved via specific torque shafts, as shown. **(c)** Many springs can be coupled in series by alternating the **(a)** and **(b)** configurations, allowing a theoretically unlimited range of deflection.

1) The design of two separate series-connection architectures that can be coupled to eliminate all prior deflection limits.
2) A nonlinear analytical model of the spring deflection profile to account for backlash in the series spring connections.
3) An empirical evaluation of the stiffness of different combinations of series springs, demonstrating the effectiveness of the design in achieving a wide range of stiffness coefficients.
4) A detailed analysis of the effect of manufacturing tolerances on design feasibility and spring backlash.

Together, these contributions aim to advance the field of mechanical design by unlocking the deflection limitation for a highly compact and lightweight torsion spring. We believe the two-part torsion spring design leverages advancements in manufacturing to enable simple, compact torsion springs without deflection limitations. These springs can be incorporated in designs across applications where mass, volume, and efficiency are design-driving factors.

## II. METHODS

### A. Mechanical Design

The spring configurations presented in this work build on our prior two-part torsion spring architecture [10] by developing two approaches for their series implementation. The original two-part design consists of a ring of radially-oriented cantilevered flexures, joined by a common outer rim. The inward-facing tips of the flexures interface with a gear-like camshaft, which bends the flexures and loads the spring when rotated. Thus, elasticity is achieved between rigid attachments to the camshaft and the outer rim. Prior work demonstrated linearity of the torque-deflection curve as well as strong alignment between modeled and measured behavior, and presented an openly available software tool to facilitate spring design customization [11]. In this work, we take a modular approach to connect multiple springs in series by either enforcing a shared outer rim or a shared central shaft (Fig. 2).

There are two potential options for the structure of the series spring implementation. These options depend on whether the joining connection between the series springs occurs on the rim of the spring disk or on the central shaft (*i.e.*, the camshaft). The first option for a series configuration involves rigidly joining the outer rims of the two springs and transferring torque between the input shaft and the output shaft (Fig. 2a). Since the camshafts have a much smaller diameter than the outer rim, this configuration allows more compact attachments and therefore a more compact assembly. When torque is applied to the input camshaft, the spring flexures

are deflected relative to the outer rim. The load is transferred to the following spring via the rigid connection at the outer rim of the assembly. This same torque is then transmitted to the output shaft via the flexures of the second spring. Two types of spacers were used to reduce friction and avoid cross-engagement of the camshafts: first, we include a small aluminum spacer on the outer rim between the two springs to reduce friction. Second, a low-friction plastic spacer—with a diameter greater than the camshafts—was placed between the two springs to ensure that both shafts can rotate easily. Lastly, we used a low-friction plastic bushing on the outer surface of the springs to support the freely rotating joined spring rims and ensure concentricity, therefore enhancing the stability of the system.

The alternative approach for series configuration uses a shared camshaft between the series springs, with their outer rims acting as either the input or output (Fig. 2b). Compared with the former configuration, this approach allows easier spring alignment, as both springs can be rigidly attached to concentric shafts. Furthermore, the floating camshaft can be easily aligned with a running fit on a concentric shaft that bridges the input and output. When torque is applied to the input shaft, the reaction load is transferred via rigid connection to the outer rim of the first spring. The load then travels down the first set of flexures, across the camshaft, and back up the second set of flexures to the outer rim of the second spring. A second rigid attachment transmits the full torque to the output shaft. Since the flexures deflect under load, this torque results in elasticity between the input and output shafts. Lastly, while this configuration allows easier alignment of the springs and shaft, it is less flexible to the size of the input shaft, as the connection must occur at the outer rim of the spring.

Leveraging both approaches for series connection allows an arbitrary number of springs to be connected in series (Fig. 2c), thereby eliminating design constraints involving spring deflection. In the case of three or more springs in series, consecutive springs must alternate between sharing a shaft or being rigidly connected at the outer rim. In this manner, loads are transferred via the shared rim or shaft and propagated either up or down the spring flexures to the following spring connection. Thus, for an odd number of springs, the input will be the camshaft of the first spring and the output will be the outer rim of the last spring (or vice versa). For an even number of series-connected springs, either rim-to-rim or shaft-to-shaft connections can be chosen for the input and output. As observed in both of the previously described configurations, spacers should be used to reduce frictional losses and avoid unintentional spring engagement. In addition, with three or more springs in series, both an external bushing and an internal alignment shaft are necessary to guarantee concentricity of floating springs and floating shafts, respectively. Fortunately, the volume and mass of each of these alignment features are small relative to the springs, so the overall energy density remains high. With these features in place, an arbitrary number of springs could be placed in series: whereas the original spring design limits spring deflection to roughly 0.35 rad, the series configuration now enables unconstrained deflection angles.

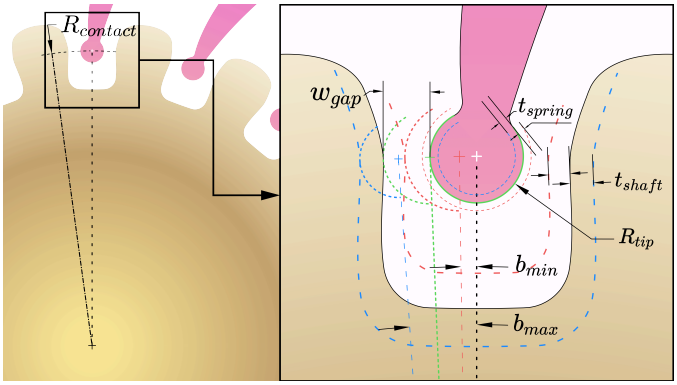


Fig. 3: Exaggerated depiction of the cam-flexure tip interface, which is the primary source of backlash. While the design gap ($w_{gap}$) and contact radius ($r_{contact}$) determine the nominal value of the backlash, tolerance on manufacturing the camshaft ($t_{shaft}$) and spring tip ($t_{spring}$) determine the boundaries of backlash values ($b_{min}$ and $b_{max}$).

### B. Backlash Compensation

Since the total backlash is magnified by the number of series connections, it must be well understood and addressed for high-performance applications. The backlash effect arises from imperfect manufacturing tolerances that require a designed air gap to ensure proper meshing between the camshaft and flexure tips. While the gap is small, it causes a momentary delay in the transmission of torque when the loading direction changes, which in turn can result in a loss of precision and control in the system. Though the backlash was imperceptible in the original camshaft-spring interface [10], it becomes more obvious with springs in series, as the series connection multiplies the number of camshaft-spring interfaces. Therefore, systems that rely on measurements of spring deflection to estimate applied torque must account for this nonlinearity to achieve high levels of precision and performance.

Prior knowledge of the designed geometry and manufacturing tolerances enables estimates of the theoretical range of backlash values (Fig. 2). More specifically, one must know the manufacturing process tolerance for both the spring ($t_{\text{spring}}$) and the shaft ($t_{\text{shaft}}$), as well as the designed air gap from the flexure tip to both neighboring cam teeth ($w_{\text{gap}}$) and the contact radius ($r_{\text{contact}}$). With these values, the minimum possible distance between the flexure tip and the opposite cam tooth (when one side is in contact) is calculated by subtracting both tolerances from the total designed air gap ($d_{\text{des}} = 2 \cdot w_{\text{gap}}$):

$$d_{\text{min}} = 2(w_{\text{gap}} - t_{\text{spring}} - t_{\text{shaft}}). \tag{1}$$

Since $d_{\text{min}}$ would ideally be equal to zero, $w_{\text{gap}}$ should typically be designed as the sum of the two tolerances. Then, with a known $w_{\text{gap}}$, the maximum possible distance between the flexure tip and cam teeth can be calculated similarly:

$$d_{\text{max}} = 2(w_{\text{gap}} + t_{\text{spring}} + t_{\text{shaft}}). \tag{2}$$

With a known contact radius, the anticipated backlash ($b$) can then be calculated for both the minimum (using $d_{\text{min}}$) and maximum (using $d_{\text{max}}$) scenarios:

$$b = 2 \cdot \arctan\left(\frac{d}{2 \cdot r_{\text{contact}}}\right) \tag{3}$$

In this work, we designed the spring and cam geometry using the default tip-to-cam gap ($w_{\text{gap}}$) setting in the openly available software design tool [11], which is 0.025 mm on both sides of the flexure tip. For electrical discharge machining (EDM), typical manufacturing tolerances range from ± 0.01 - 0.05 mm. Assuming the shaft and spring both have a tolerance of ± 0.03 mm, $d_{\min}$ would be -0.07 mm, and $d_{\max}$ would be 0.17 mm. Using the contact radius from this work (5.5 mm), the expected backlash would then fall within the range of [-0.0127, 0.0309] rad. The negative lower end of the range indicates the possibility that the camshaft will interfere with the spring and thus be unusable; hence, it is important to be familiar with the capabilities of the intended manufacturer when trying to minimize the backlash.

*1) Deadband Model:* Despite the possibility of substantial backlash, accurate estimates of spring torque can still be obtained with an appropriate backlash model. A deadband model assumes zero torque within the backlash regime and is presented below, where $K$ is the linear stiffness and $h$ is half the total backlash ($h = b/2$):

$$\tau = \begin{cases} K(\theta - h) & \theta \in (h, +\infty) \\ 0 & \theta \in [-h, h] \\ K(\theta + h) & \theta \in (-\infty, -h). \end{cases} \tag{4}$$

To determine both $K$ and $b$, we include this model in a higher-level optimization, which constrained $b$ to be centered at zero radians and enforced the same $K$ for both positive and negative loading directions. The objective function minimized the sum of the absolute error between the model and the measured torque-deflection relationship. In addition to parameterizing this model, the optimized values of $K$ and $b$ were used to quantify the average measured stiffness and backlash, respectively, for each series configuration. Overall, this model improves torque estimation accuracy, but also results in sharp changes in measured torque at the edge of the backlash region, which could add challenge for some feedback controllers.

*2) Logit Model:* A more complex model fits a logit function to the zero-torque crossover region to avoid discontinuities and allow smooth progression of torque estimates. Early empirical testing indicated that a logit function centered at $(0, 0)$ may better describe the crossover behavior:

$$f(x) = g \ln \frac{1 + 2cx}{1 - 2cx}, \tag{5}$$

where $c$ and $g$ are scaling parameters. Since stiffness ($K$) scales the angle linearly, backlash compensation can be thought of as a transformation from measured angle difference ($\theta_{\text{diff}}$) to spring deflection angle ($\theta_{\text{spring}}$). In this case, the non-backlash regions should have a slope of one. With the crossover region defined as $\theta_{\text{diff}} \in [-(h + l), h + l)]$, where $l$ is a transition region, boundary conditions can then be defined as:

$$f(h + l) = l, \tag{6}$$

$$f'(h + l) = 1. \tag{7}$$

Thus, for a given $l$, $c$ and $g$ can be calculated to ensure that the piecewise transition is continuous. With only a single degree of freedom for the set of equations, $l$ can then be optimized to achieve the closest match to the measured relationship. The full torque estimate can then be modeled by the following equation:

$$\tau = K \cdot \theta_{\text{spring}} \tag{8}$$

where

$$\theta_{\text{spring}} = \begin{cases} \theta_{\text{diff}} - h & \theta_{\text{diff}} \in (h + L, \infty) \\ g \ln \left( \frac{1+2c\theta_{\text{diff}}}{1-2c\theta_{\text{diff}}} \right) & \theta_{\text{diff}} \in [-(h + L), h + L] \\ \theta_{\text{diff}} + h & \theta_{\text{diff}} \in (-\infty, -(h + L)) \end{cases} \tag{9}$$

This representation eliminates discontinuities, but does require empirical testing in order to properly fit the model parameters.

### C. Hardware Testing

To validate the series connection and demonstrate its potential, we designed several unique series configurations and evaluated their performance in a physical hardware implementation. All tested configurations consisted of two distinct spring designs (S1 and S2), both generated by the previously referenced spring software design tool [11] to simplify the design process and enable easy replication. The stiffness for S1 (150 $\frac{\text{N·m}}{\text{rad}}$) was selected to facilitate direct comparison to prior work [10]. Since a large portion of this work involves verification of the series stiffness, we designed the stiffness of S2 (75 $\frac{\text{N·m}}{\text{rad}}$) such that two S1 springs in series should yield identical stiffness to a single S2 spring. To explore a large design space, we obtained four S1 springs and two S2 springs. All six springs and their corresponding camshafts were manufactured from heat-treated 420 stainless steel with wire electronic discharge machining (EDM). Importantly, we constrained the number of flexures, flexure tip radius, contact radius and outer radius in the design tool to ensure that the same camshaft and housing were compatible with both springs. This enabled comparisons of 75, 37.5, and 30 $\frac{\text{N·m}}{\text{rad}}$ stiffness coefficients, each achieved with two different series configurations.

For empirical characterization of the stiffness and deflection properties of each series-spring configuration, we constructed

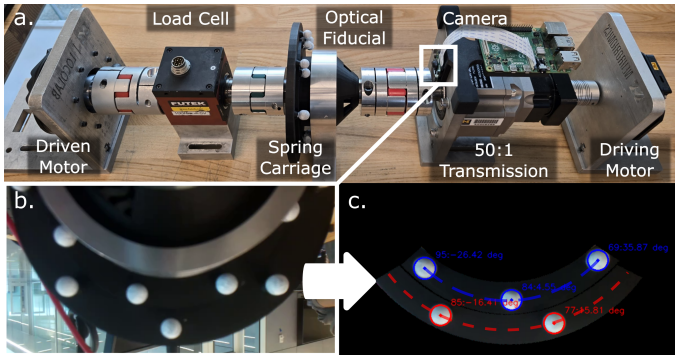


Fig. 4: Testbed setup used to measure the properties of each series-spring configuration. **(a)** True deflection of the spring architecture is indicated by two arrays of optical fiducials and recorded by the camera, while the transmitted torque is measured by the serial load cell. **(b)** Camera view of the optical fiducials. **(c)** Masked view of camera frame, where each fiducial is tracked along a fitted ellipse to determine angle about the center of rotation.

a benchtop testing apparatus to measure applied torque and the resulting spring deflection (Fig. 4). The input and output of the spring assembly were each coupled to a brushless DC motor (ActPack, Dephy Inc., Boxborough, MA, USA) to allow either independent or synchronous rotary motion. The transmitted torque was measured by a non-contact sensor (TRS605, Futek, Irvine, CA, USA) placed in series with the spring assembly. The analog output voltage from the torque sensor was sampled by a 16-bit analog-to-digital converter (ADS1115, Texas Instruments, Dallas, TX). All control commands and sensor readings were implemented on a microprocessor (RPi 5, Raspberry Pi Foundation, Cambridge, U.K.) running and recording data at 500 Hz. While both actuators supply reliable angular positions, the compliance of the connecting shafts and couplers resulted in a substantial difference between the measured encoder deflection and the actual spring deflection. Thus, similar to [10], we implemented an optical measurement of spring deflection in order to obtain reliable measurements and accurately assess spring stiffness.

The optical measurement strategy used a camera to track two fiducial arrays to accurately measure spring deflection. The two arrays of optical fiducials were placed on the input and output of the spring assembly to eliminate unintended series compliance between the fiducials and springs. The camera (RPi Camera Module 2, Raspberry Pi Foundation, Cambridge, U.K.) captured video of the rotating fiducials at 60 frames per second, and the relative deflections of the two arrays were calculated offline. The recorded video was processed by first masking the image to isolate the known region containing fiducials. We then used OpenCV [12] to track the individual fiducials across successive frames. Using frames with at least 3 fiducials present, we fit an ellipse to calculate the rotation about a center point, and measured the spring deflection as the relative difference in rotation between the first and second fiducial arrays. This approach alone was not sufficiently accurate, with measured errors of (-1.37 (SD=0.27))$\times 10^{-2}$ rad and (-4.11 (SD=0.49))$\times 10^{-2}$ rad for the outer and inner sets of fiducials, respectively. Consequently, we implemented a second-stage calibration to improve tracking accuracy. Under no load, the motor encoder angles should progress one-to-one with the camera-measured angles. Thus, we recorded both sets of angles during a calibration routine to create a secondary mapping from camera-measured angles to known encoder angles. With this update, the measured errors were reduced to (2.99 (SD=1.15))$\times 10^{-3}$ rad and (5.11 (SD=0.43))$\times 10^{-3}$ rad for the outer and inner fiducial arrays, respectively. The calibration consisted of two full rotations in both directions—with both motors spinning synchronously to avoid any load along the shaft—and was performed before each test to ensure the secondary mapping was properly centered about the testing equilibrium.

*1) Testing Protocol:* Testing consisted of alternating ramped position trajectories that increased to a predetermined maximum. For each series spring configuration, one motor was swapped for a mechanical ground while the other motor started at equilibrium, ramped up to a predetermined position target, and returned to equilibrium before immediately repeating the trajectory in the negative direction. The position target started at four degrees and then increased in four-degree increments to 24 degrees. For some configurations, we ramped up to the maximum allowable deflection ($\Delta\theta_{max}$) of the configuration, as determined by the design limits ($\Delta\theta_{max,i}$) and stiffness ($K_i$) of each constituent spring:

$$\Delta\theta_{max} = \min_{\forall i \in [1,n]} (\Delta\theta_{max,i} K_i) \cdot \sum_{i=1}^{n} \left( \frac{1}{K_i} \right) \tag{10}$$

As mentioned, we tested two spring configurations at each of the following nominal stiffness targets: 75, 37.5 and 30 $\frac{\text{N·m}}{\text{rad}}$. The specific spring combinations for each stiffness can be seen in Tab. I, where we also present the baseline stiffness of the S1 spring.

*2) Manufacturer Comparison:* To investigate the sensitivity of the spring performance to the manufacturer, we ordered one complete set of six springs from each of two separate manufacturers (Mfr. 1[1] and Mfr. 2[2]). Testing was performed on both sets of springs to elucidate differences in spring performance

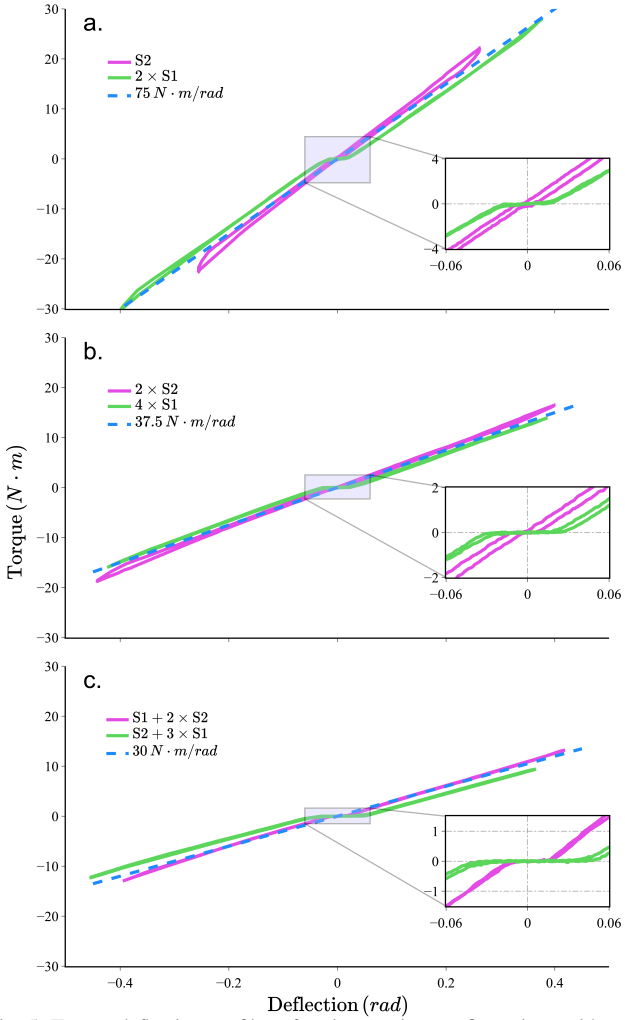


Fig. 5: Torque-deflection profiles of various spring configurations with target stiffnesses of a) 75 $\frac{\text{N·m}}{\text{rad}}$, b) 37.5 $\frac{\text{N·m}}{\text{rad}}$, and c) 30 $\frac{\text{N·m}}{\text{rad}}$. The detailed views show the zero-torque crossover region, where backlash increases with the number of springs in series.

[1]Zintilon Co., Limited, https://www.zintilon.com/

[2]Star Rapid Manufacturing, https://www.starrapid.com/

| Target Spring Stiffness ($\frac{\text{N·m}}{\text{rad}}$) | Configuration | Maximum Deflection Limit (rad) | Tested Range of Deflection (rad) | Measured Spring Stiffness ($\frac{\text{N·m}}{\text{rad}}$) | Percent Stiffness Error (%) | Linear Fit NRMSE (mean%) | Deadband Model NRMSE (mean%) | Logit Model NRMSE (mean%) | Backlash (rad) | Percent Energy Loss (%) |
|---|---|---|---|---|---|---|---|---|---|---|
| 150 | **S1** | 0.279 | 0.279 | 161.11 | +7.41 | 6.42 | 3.71 | 3.75 | $1.13 \times 10^{-2}$ | 12.94 |
| 75 | **S2** | 0.349 | 0.279 | 86.12 | +14.82 | 4.53 | 3.13 | 3.13 | $1.15 \times 10^{-2}$ | 9.11 |
| | $\mathbf{2 \times S1}$ | 0.559 | 0.419 | 76.94 | +2.59 | 5.82 | 1.28 | 1.27 | $3.29 \times 10^{-2}$ | 1.32 |
| 37.5 | $\mathbf{2 \times S2}$ | 0.698 | 0.419 | 41.69 | +11.17 | 7.05 | 3.84 | 3.82 | $1.64 \times 10^{-2}$ | 5.64 |
| | $\mathbf{4 \times S1}$ | 1.117 | 0.419 | 39.21 | +4.56 | 16.06 | 10.76 | 10.74 | $5.98 \times 10^{-2}$ | 2.81 |
| 30 | $\mathbf{S1 + 2 \times S2}$ | 0.977 | 0.419 | 32.31 | +7.70 | 3.27 | 2.12 | 2.12 | $2.85 \times 10^{-2}$ | 0.90 |
| | $\mathbf{S2 + 3 \times S1}$ | 1.187 | 0.419 | 31.87 | +6.23 | 6.72 | 1.92 | 1.92 | $4.91 \times 10^{-2}$ | 4.70 |

TABLE I: The performance of each modular torsion spring configuration is presented across various categories (all from Mfr. 2). Maximum deflection was governed by the constituent springs in each configuration (10), but not all configurations were tested to their limit. Spring stiffness was calculated as the slope ($K$) of the deadband model, and the percent stiffness error is based on that value relative to the target stiffness. We used the NRMSE (with normalization by half of the peak torque) to quantify the fitness of each model to the measured data. Lastly, we assessed the backlash (defined as the crossover region in (4)), and the percent energy loss (energy lost across one loading-unloading cycle compared to energy stored on one loading cycle).

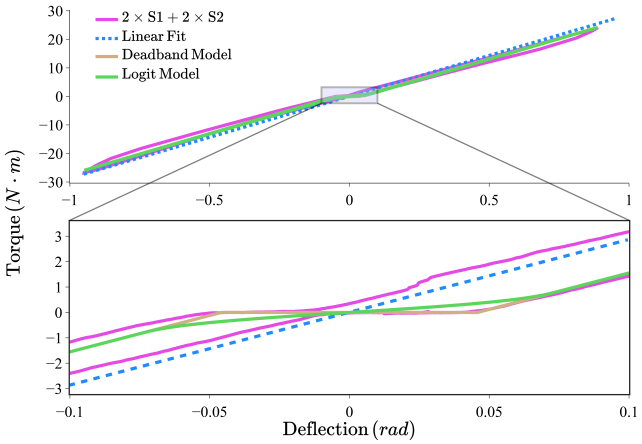


Fig. 6: Torque-deflection profile of one series-spring configuration with corresponding model fits. Compared to the simple linear fit, the deadband and logit models account for backlash with a piecewise horizontal offset. Whereas the deadband model assumes zero torque in the gap, the logit model fits a parametric logit function to guarantee continuity in the torque estimate.

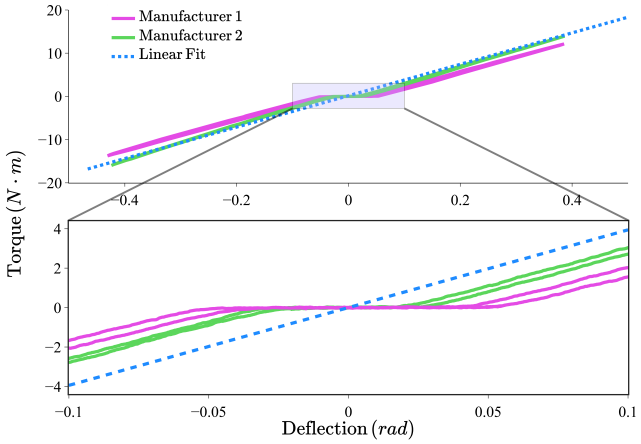


Fig. 7: Comparison of backlash across two manufacturers for the same spring design and configuration. Both versions achieve the target stiffness, but the Mfr. 1 springs show a considerable increase in backlash when compared to Mfr. 2.

with respect to the provided manufacturing accuracy from the manufacturers.

## III. RESULTS

The tested spring configurations closely matched the expected stiffness coefficients, with notable backlash in some configurations (Tab. I). Torque-deflection trajectories for $\pm 0.279$ or $\pm 0.419$ radian loading cycles are shown for the single spring and series spring configurations, respectively, at each of the nominal stiffness targets (Fig. 5). The average stiffness of each configuration (II-B1) matched the target value within 2-15%, demonstrating close alignment with modeled behavior across various spring configurations. While the peak torque was not tested for every configuration, Fig. 6 demonstrates a consistent response at the designed deflection limits of $\pm 1$ radian. The measured backlash values were substantial, ranging from $1.13 \times 10^{-2}$ to $5.98 \times 10^{-2}$ radians, with a total average of 0.0123 radians per spring-cam interface. Notably, the percent energy loss was only 1-6% for series spring configurations, while the individual springs suffered a larger percentage loss of 9-13%.

The two backlash models used in our approach resulted in significant improvements in torque estimation when compared to simple linear approximation. To quantify the fitness of our backlash models, the NRMSE was calculated as the root mean squared error (RMSE) in torque between the models and the measured trajectory, with normalization implemented according to the range of measured torque values for each respective trajectory. The NRMSE for the linear fits ranged from 3 - 16% (RMSE: 0.43 - 2.5 Nm) across all configurations, with the deadband and logit models ranging from 1 - 11% (RMSE: 0.23 - 1.46 Nm). While the logit model qualitatively behaves similarly to the measured profiles (Fig. 6), the difference in NRMSE between the deadband and logit models was minimal.

TABLE II: Performance of $\mathbf{4 \times S1}$ configuration for both manufacturers

| Manufacturer | Target Stiffness ($\frac{\text{N·m}}{\text{rad}}$) | Measured Stiffness ($\frac{\text{N·m}}{\text{rad}}$) | Max. Expected Backlash (rad) | Measured Backlash (rad) |
|---|---|---|---|---|
| Mfr. 1 | 37.5 | 36.09 | $9.44 \times 10^{-2}$ | $9.96 \times 10^{-2}$ |
| Mfr. 2 | 37.5 | 39.44 | $13.8 \times 10^{-2}$ | $5.98 \times 10^{-2}$ |

Comparison of spring configurations from the two different

manufacturers demonstrated a significant difference in the measured backlash (Fig. 7, Tab. II). Upon request, both manufacturers (Mfr. 1 vs. Mfr. 2) provided the machine tolerances for $t_{\text{shaft}}$ (0.03 mm vs. 0.02 mm) and $t_{\text{spring}}$ (0.01 mm vs. 0.05 mm). Based on the designed geometry and these reported values, the expected backlash for each single spring was $0.91 \times 10^{-2}$ radians, $\pm 1.45 \times 10^{-2}$ or $\pm 2.54 \times 10^{-2}$ radians for Mfr. 1 or 2, respectively. The measured backlash for a single spring ranged from $2.49 \times 10^{-2}$ radians for the springs from Mfr. 1, down to $1.50 \times 10^{-2}$ for the springs from Mfr. 2. Despite these differences in backlash, the measured stiffness coefficients were consistent across both manufacturers, with the percent stiffness error from the designed value (37.5 $\frac{\text{N·m}}{\text{rad}}$) to be -3.77% and 5.16%, for the Mfr. 1 and 2 configurations, respectively.

## IV. DISCUSSION

In this article, we introduced series design implementations of an emerging two-part torsion spring design. While the two-part design had among the highest specific energy and energy density in the literature, the spring's use was constrained by deflection limitations inherent in the design. We have overcome this limitation with the series spring architecture presented (Fig. 8). The series design implementation includes multiple options for series connection—depending on the desired mechanics—with the possibility for arbitrarily large deflection ranges by placing multiple springs in series. With hardware testing, we demonstrated accurate rendering of desired stiffness within 2 - 15% across several configurations, ranging from 25 - 150 $\frac{\text{N·m}}{\text{rad}}$. Higher stiffness coefficients and larger deflections are also feasible by simply adjusting the individual spring design and the number of spring disks in series. In addition, the hysteresis remained low (5.3% average energy loss), indicating the potential of this torsion spring architecture to excel in high-efficiency energy storage and release applications. Overall, this work aligns well with our previous studies investigating compact and lightweight torsion springs [10], [13] while eliminating the prior constraint on the total possible deflection.

Despite increased componentry, the series architectures of the two-part torsion spring remain the most energy-dense torsion springs in the field to our knowledge. Based on previous results, the base spring design used in our prior work can achieve an energy density in the range of 0.30 (SD=0.05) $\frac{\text{J}}{\text{cm}^3}$, compared to an average of 0.11 (SD=0.10) $\frac{\text{J}}{\text{cm}^3}$ in the literature [10]. The series springs in this work range from 0.24 – 0.39 $\frac{\text{J}}{\text{cm}^3}$, demonstrating the potential for this design to serve as a compact spring unit. Interestingly, the measured specific energy of the series springs (31 – 52 $\frac{\text{J}}{\text{kg}}$) was much closer to the literature average (29 (SD=23) $\frac{\text{J}}{\text{kg}}$) than the prior base spring results (68 (SD=5) $\frac{\text{J}}{\text{kg}}$). While we did expect the specific energy of the series configuration to decrease due to the presence of additional components, the decrease is exacerbated by the thick outer rim (see Fig. 2a), which allows the springs to be easily assembled with fasteners. Disassembly was important for this work to allow rearrangement of the springs in multiple configurations for testing purposes, but for a longer-term application, a more permanent fixturing method (*e.g.*, spring pins) could be used and allow for a thinner outer rim while still providing the necessary connection interface. Based on CAD models, reducing the rim to a more representative thickness would result in a roughly 20% increase in specific energy, with an anticipated range of 37 – 63 $\frac{\text{J}}{\text{kg}}$: much closer to the previously measured range for the base spring design. While 37 $\frac{\text{J}}{\text{kg}}$ is considerably lower than previous values, it is partially due to the configuration comprising both S1 and S2 springs: since the combination can only be loaded to the peak torque of the weaker spring (S2), the two S1 springs cannot be fully loaded without yielding the S2 springs (10); thus the mass of S1 is underutilized. Overall, the series spring architecture is highly energy dense and greater specific energy can be achieved by minimizing the thickness of the outer rim and utilizing springs with more similar peak torque specifications.

While manufacturing precision has a minimal effect on spring stiffness, it can meaningfully impact assembly backlash. Based on the tolerances provided by the manufacturers, the expected backlash range was larger for Mfr. 2 ($(0.91 \pm 2.54) \times 10^{-2}$ rad) than for Mfr. 1 ($(0.91 \pm 1.45) \times 10^{-2}$ rad); however, the measured results indicate that the Mfr. 2 springs ($1.50 \times 10^{-2}$ rad) had nearly half the backlash of the Mfr. 1 springs ($2.49 \times 10^{-2}$ rad). Importantly, while the measured backlash values remained within the expected bounds for Mfr. 2, the springs from Mfr. 1 had a higher average backlash than the expected upper limit for the Mfr. 1 tolerances ($2.49 \times 10^{-2}$ rad vs $2.36 \times 10^{-2}$ rad); thus, the large backlash for the Mfr. 1 springs is likely due to manufacturing errors. Irrespective of manufacturer, both sets of springs exhibited significantly larger backlash than observed in previous studies [10], [13], despite the previous springs being manufactured with the same specified tolerances and by one of the same manufacturers (Mfr. 2). Since both measured backlash values are close to the possible specified range, it is possible that the difference can be explained by typical tool drift over time or stochastic variance in machine accuracy; however, one distinct difference in design is that previous work specified a flexure-tip radius of 0.375 mm, compared to 0.300 mm for the springs

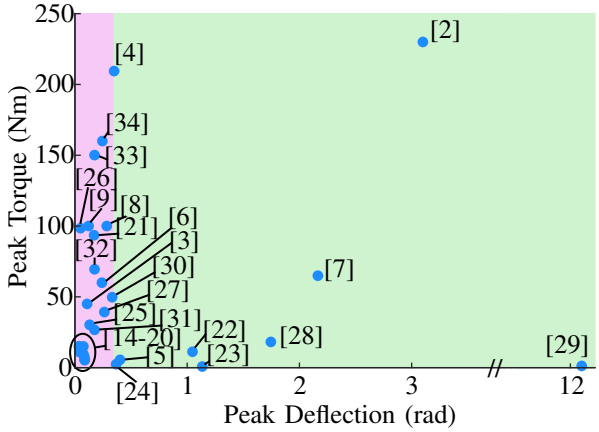


Fig. 8: Peak torque and deflection from various published torsion spring designs. The pink shaded region represents designs that could be replicated by our prior study, whereas green represents the expansion of the design space based on this work. Several springs were designed for low torque and deflection applications [14]–[20], while the others span a wide range of the design space [2]–[4], [6]–[9], [21]–[34].

presented here. While the difference is small, the consistent difference between backlash values across the current prototypes and previous versions may indicate that larger features can be more accurately reproduced. For reference, the backlash values measured in this work fall within common ranges ($(1.0 - 3.7)\times10^{-2}$ rad) for planetary gearsets [35], [36], but regardless, any amount of backlash is undesirable and should be appropriately mitigated and addressed. Possible strategies for reducing backlash in future work include maximizing the contact radius (so that a given gap results in smaller angular deviation) and designing larger interfacing features (such as the tip radius) that can be manufactured with higher repeatability.

The proposed backlash models drastically reduce measurement error and could facilitate a robust closed-loop torque control framework. Compared to a simple linear scaling of deflection, both backlash models (deadband and logit) improve the overall fit of the torque estimator by an average of 50%. When comparing NRMSE across the full deflection range, the logit model (nonlinear piecewise) has a slightly better fit than the deadband model (linear piecewise); however, the logit model importantly has a continuous crossover region which would allow improved control around zero torque. To our knowledge, a logit model such as that proposed here has not been previously used to compensate for backlash in spring systems. While it is possible that the observed logit behavior is unique to our setup, we believe that it could be a useful approach to modeling a wider range of nonlinear systems.

While the present work provides valuable groundwork for the design of compact, high-deflection springs, future work is needed to maximize the potential of this design architecture. First, not all spring configurations were tested to peak designed deflection. This was in part due to the primary focus of comparing the stiffness of several configurations across a consistent deflection range; however, both configurations that were tested to full deflection (S1 and 2×S1+2×S2) exhibited a consistent linear profile throughout the full deflection range. Second, some configurations exhibited a zero-torque angular offset between the loading and unloading point (*e.g.*, Fig. 6). This behavior was observed in one of the springs reported in our previous work [10], and is likely due to hysteretic losses. Future work could investigate this (and other) possible explanations for the observed behavior. Lastly, while the backlash models do provide significant improvements in torque-estimation, fitting the model parameters relies on some level of system characterization, which can be undesired for certain applications.

The two-part torsion spring presented in [10], [13] shows potential for compact, lightweight elasticity that can be useful, especially in robotic applications. We have extended the functionality of this torsion spring architecture by developing and characterizing a series configuration. Our prior design was limited by the total allowable deflection, but we have overcome this limitation to enable greater allowable deflections. By adding springs in series, we are able to adjust a new dimension in the torsion-spring design space, allowing lightweight replication of numerous springs across a variety of applications (Fig. 8). This work offers the potential for more lightweight and more compact springs and devices: even those requiring large ranges of deflection.

## V. CONCLUSION

In this work, we introduced and experimentally validated a series-connected torsion spring architecture that transcends the deflection limitation of our prior work. By leveraging modular series connections, our approach enables designers to combine multiple springs to achieve arbitrarily large total deflections and finely tunable stiffness profiles, while retaining high specific energy and energy density. Our empirical investigation demonstrated that the proposed system offers predictable stiffness, and our analytical spring models allowed effective torque prediction despite non-negligible backlash. This design paradigm enables new possibilities for developing lightweight, customizable, and efficient spring-based actuation in robotics, automotive mechanisms, and other fields requiring large displacement, compliant motions. Future work may focus on optimizing component tolerances and further reducing backlash.

## REFERENCES


[1] G. A. Pratt and M. M. Williamson, "Series elastic actuators," *IEEE International Conference on Intelligent Robots and Systems*, vol. 1, pp. 399–406, 1995.

[2] J. M. Muñoz-Guijosa, D. F. Caballero, V. R. D. L. Cruz, J. L. M. Sanz, and J. Echávarri, "Generalized spiral torsion spring model," *Mechanism and Machine Theory*, vol. 51, pp. 110–130, 5 2012.

[3] O. S. Al-Dahiree, R. A. R. Ghazilla, M. O. Tokhi, H. J. Yap, and M. Gul, "Design and characterization of a low-cost and efficient torsional spring for es-rsea," *Sensors*, vol. 23, 4 2023.

[4] N. Georgiev and J. Burdick, "Design and analysis of planar rotary springs," *IEEE International Conference on Intelligent Robots and Systems*, vol. 2017-Septe, pp. 4777–4784, 2017.

[5] C. H. Huang and C. C. Lan, "High-torque-capacity helical flexures for series elastic actuators," *IEEE/ASME Transactions on Mechatronics*, 2025.

[6] D. Accoto, G. Carpino, F. Sergi, N. L. Tagliamonte, L. Zollo, and E. Guglielmelli, "Design and characterization of a novel high-power series elastic actuator for a lower limb robotic orthosis," *International Journal of Advanced Robotic Systems*, vol. 10, 2013.

[7] B. T. Knox and J. P. Schmiedeler, "A unidirectional series-elastic actuator design using a spiral torsion spring," *Journal of Mechanical Design, Transactions of the ASME*, vol. 131, pp. 1 250 011–1 250 015, 2009.

[8] C. Lagoda, A. C. Schouten, A. H. Stienen, E. E. Hekman, and H. V. D. Kooij, "Design of an electric series elastic actuated joint for robotic gait rehabilitation training," *Journal of Applied Rehabilitation Counseling*, vol. 4, pp. 208–223, 2010.

[9] S. Wang, C. Meijneke, and H. V. D. Kooij, "Modeling, design, and optimization of mindwalker series elastic joint," *IEEE International Conference on Rehabilitation Robotics*, 2013.

[10] Z. Bons, G. C. Thomas, L. Mooney, and E. J. Rouse, "An energy-dense two-part torsion spring architecture and design tool," *IEEE/ASME Transactions on Mechatronics*, vol. 29, pp. 2373–2384, 6 2024.

[11] The Spring Design Tool and associated source code are available at https://github.com/neurobionics/spring-design-tool.

[12] G. Bradski, "The OpenCV Library," *Dr. Dobb's Journal of Software Tools*, 2000.

[13] Z. Bons, G. C. Thomas, L. M. Mooney, and E. J. Rouse, "A compact, two-part torsion spring architecture," in *Proceedings - IEEE International Conference on Robotics and Automation*, vol. 2023-May. IEEE, 2023, pp. 7461–7467.

[14] G. Carpino, D. Accoto, F. Sergi, N. L. Tagliamonte, and E. Guglielmelli, "A novel compact torsional spring for series elastic actuators for assistive wearable robots," *Journal of Mechanical Design, Transactions of the ASME*, vol. 134, pp. 1–10, 2012.

[15] W. M. dos Santos, G. A. Caurin, and A. A. Siqueira, "Design and control of an active knee orthosis driven by a rotary series elastic actuator," *Control Engineering Practice*, vol. 58, pp. 307–318, 2015.
[16] G. G. Fiorezi, J. dos Santos de Moraes, P. H. F. Ulhoa, and R. M. de Andrade, "Biomimetic design of a planar torsional spring to an active knee prosthesis actuator using fem analysis," *Proceedings*, p. 30, 2020.
[17] T. Kim, K. Shi, and K. Kong, "A compact transmitted-force-sensing series elastic actuator with optimized planar torsional spring for exoskeletons," *IEEE/ASME International Conference on Advanced Intelligent Mechatronics, AIM*, vol. 2021-July, pp. 572–577, 2021.
[18] F. Negrello, M. G. Catalano, M. Garabini, M. Poggiani, D. G. Caldwell, N. G. Tsagarakis, and A. Bicchi, "Design and characterization of a novel high-compliance spring for robots with soft joints," *IEEE/ASME International Conference on Advanced Intelligent Mechatronics, AIM*, pp. 271–278, 2017.
[19] Y. Long, Z. J. Du, C. F. Chen, W. D. Wang, and W. Dong, "Development of a lower extremity wearable exoskeleton with double compact elastic module: Preliminary experiments," *Mechanical Sciences*, vol. 8, pp. 249–258, 8 2017.
[20] L. Wang, Z. Du, W. Dong, Y. Shen, and G. Zhao, "Intrinsic sensing and evolving internal model control of compact elastic module for a lower extremity exoskeleton," *Sensors*, vol. 18, 3 2018.
[21] S. K. Au, J. Weber, and H. Herr, "Biomechanical design of a powered ankle-foot prosthesis," in *IEEE International Conference on Rehabilitation Robotics*, 2007.
[22] R. Chaichaowarat, J. Kinugawa, and K. Kosuge, "Cycling-enhanced knee exoskeleton using planar spiral spring," *Proceedings of the Annual International Conference of the IEEE Engineering in Medicine and Biology Society, EMBS*, vol. 2018-July, pp. 3206–3211, 2018.
[23] R. Chaichaowarat, J. Kinugawa, A. Seino, and K. Kosuge, "A spring-embedded planetary-geared parallel elastic actuator," in *IEEE/ASME International Conference on Advanced Intelligent Mechatronics (AIM)*, 7 2020.
[24] D. Chakarov, M. Tsveov, I. Veneva, and P. Mitrouchev, "Adjustable compliance joint with torsion spring for human centred robots," *International Journal of Advanced Robotic Systems*, vol. 12, 12 2015.
[25] Y. Chen, Y. Huang, K. Chen, Y. Wang, and Y. Wu, "Novel torsional spring with corrugated flexible units for series elastic actuators for cooperative robots," *Journal of Mechanical Science and Technology*, vol. 36, pp. 3131–3142, 6 2022.
[26] P. Herodotou and S. Wang, "Design, modelling, and experimental evaluation of a compact elastic actuator for a gait assisting exoskeleton," *IEEE International Conference on Rehabilitation Robotics*, vol. 2019-June, pp. 331–336, 2019.
[27] T. Kamioka, H. Shin, R. Yamaguchi, and M. Muromachi, "Development and analysis of a biped robot with prismatic compliance," in *IEEE International Conference on Robotics and Automation*. IEEE, 2022, pp. 10 398–10 404.
[28] Y. H. Lee, L. T. Phan, D. Y. Kim, H. Lee, J. C. Koo, and H. R. Choi, "Biologically inspired robotic leg for high-speed running," in *IEEE International Conference on Advanced Intelligent Mechatronics (AIM)*. IEEE, 2016, p. 1705.
[29] A. Silva, G. López-Navarrete, C. García-Martos, and J. M. Muñoz-Guijosa, "Automated resolution of the spiral torsion spring inverse design problem," *Scientific Reports*, vol. 14, 12 2024.
[30] A. H. Stienen, E. E. Hekman, H. T. Braak, A. M. Aalsma, F. C. V. D. Helm, and H. V. D. Kooij, "Design of a rotational hydroelastic actuator for a powered exoskeleton for upper limb rehabilitation," *IEEE Transactions on Biomedical Engineering*, vol. 57, pp. 728–735, 2010.
[31] N. G. Tsagarakis, M. Laffranchi, B. Vanderborght, and D. G. Caldwell, "A compact soft actuator unit for small scale human friendly robots," in *IEEE International Conference on Robotics and Automation*. IEEE, 2009, pp. 4356–4362.
[32] T. Zhang and J. Xia, "Development of a clutchable series elastic actuator for robotic hip exoskeleton," in *IEEE Conference on Cybernetics and Intelligent Systems (CIS) and Robotics, Automation and Mechatronics (RAM)*. IEEE, 2019.
[33] S. Yoo, J. Lee, J. Choi, G. Chung, and W. K. Chung, "Development of rotary hydro-elastic actuator with robust internal-loop-compensator-based torque control and cross-parallel connection spring," *Mechatronics*, vol. 43, pp. 112–123, 2017.
[34] S. Wolf and G. Hirzinger, "A new variable stiffness design: Matching requirements of the next robot generation," in *IEEE International Conference on Robotics and Automation*. IEEE Xplore, 2008.
[35] Y. Ding and H.-W. Park, "Design and experimental implementation of a quasi-direct-drive leg for optimized jumping," in *IEEE/RSJ International Conference on Intelligent Robots and Systems*, 2017.
[36] T. Elery, S. Rezazadeh, C. Nesler, and R. D. Gregg, "Design and validation of a powered knee-ankle prosthesis with high-torque, low-impedance actuators," *IEEE Transactions on Robotics*, vol. 36, pp. 1649–1668, 12 2020.

**Zachary Bons** (S'21) received the B.S. degree in mechanical engineering from Brigham Young University, Provo, UT, USA, in 2021. He is currently a member of the Neurobionics Lab and PhD candidate in Mechanical Engineering at the University of Michigan, Ann Arbor, MI, USA. His research interests include the design, development and control of robotic exoskeletons and prostheses with the purpose of improving mobility and quality of life.

**Yuanshao Yang** received the B.S. degree from the University of Michigan in 2025. He was a member of the Neurobionics Lab as an undergraduate research intern, and he is currently pursuing a PhD degree at the Georgia Institute of Technology. His research interests include actuation mechanism design, and the control strategies in robotic prostheses and exoskeletons, aiming to reduce the metabolic cost of walking for people with locomotor disabilities.

**Elliott J. Rouse** (S'10, M'12, SM'20) received the B.S. degree in mechanical engineering from The Ohio State University, Columbus, OH, USA, in 2007, the M.S. and Ph.D. degrees in biomedical engineering from Northwestern University, Evanston, IL, USA, in 2009 and 2012. Afterwards, he joined the Massachusetts Institute of Technology, Cambridge MA, USA as a postdoctoral fellow until 2014. He is currently an Associate Professor at the University of Michigan, Ann Arbor, MI, USA in the Departments of Robotics and Mechanical Engineering. Prior to joining the University of Michigan, he was faculty at the Shirley Ryan AbilityLab / Northwestern University, Chicago, IL, USA. His research interests include precision machine design, control, biomechanical modeling, psychophysics, and the use of these tools to develop meaningful exoskeletons and robotic prostheses that advance mobility and quality of life.